Chinese Chemical Letters 36 (2025) 109937

Contents lists available at ScienceDirect

Chinese Chemical Letters

journal homepage: www.elsevier.com/locate/cclet

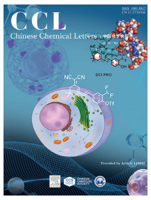

Auto-tandem CO_2 reduction by reconstructed Cu imidazole framework isomers: Unveiling pristine MOF-mediated CO_2 activation

Xiang-Da Zhang[a,1], Jian-Mei Huang[a,1], Xiaorong Zhu[b,1], Chang Liu[a], Yue Yin[a], Jia-Yi Huang[a], Yafei Li[a,*], Zhi-Yuan Gu[a,*]

[a] *Jiangsu Key Laboratory of Biofunctional Materials, Jiangsu Collaborative Innovation Center of Biomedical Functional Materials, Jiangsu Key Laboratory of New Power Batteries, College of Chemistry and Materials Science, Nanjing Normal University, Nanjing 210023, China*
[b] *School of Chemistry and Chemical Engineering, Nantong University, Nantong 226019, China*

ARTICLE INFO

Article history:
Received 8 March 2024
Revised 2 April 2024
Accepted 28 April 2024
Available online 29 April 2024

Keywords:
CO_2 reduction reactions
Cu-based MOF
In-situ reconstructed
Coordination environment
Auto-tandem catalysis

ABSTRACT

Cu-based metal-organic frameworks (MOFs) are widely employed in CO_2 reduction reactions (CO_2RR). Mostly, the *in-situ* reconstructed derivatives such as Cu or Cu oxides during CO_2RR are regarded as the catalytic active center for the formation of catalytic products. However, in many cases, the pristine MOFs still exist during the catalytic process, the key role of these pristine MOFs is often ignored in revealing the catalytic mechanism. Here, we designed two Cu(imidazole) with different coordination environments, namely CuN_2 and Cu_2N_4 for CO_2RR. The structures of the two MOFs were still remained after the catalytic reaction. We discovered that the pristine MOFs served as activation catalysts for converting CO_2 into CO. Sequentially, the Cu-based derivatives, in the two cases, Cu(111) converted the CO into C_{2+} products. The CuN_2 with more exposed Cu-N centers showed a higher FE_{CO} and a higher final FE_{C2+} than Cu_2N_4. This auto-tandem catalytic mechanism was supported by electrocatalytic performance, TPD-CO, HRTEM, SAED, XPS, *in-situ* XANES and XES and DFT computation. The auto-tandem catalytic mechanism provides a new route to design Cu-based MOF electrocatalysts for high product selectivity in CO_2RR.

Cu-based metal-organic frameworks (MOFs) have been recognized as promising catalysts in the CO_2 reduction reaction (CO_2RR) catalysts for generating of C_{2+} products [1–7]. It has been widely accepted that Cu-based MOFs usually undergo *in-situ* reconstruction, yielding Cu-base derivatives, such as Cu, Cu_2O, CuO species and their heterostructures [8–11]. These generated derivatives are identified as paramount active sites for facilitating C–C coupling in CO_2RR [11,12]. However, in many cases, distinct MOF precursors can reconstruct the same Cu-based derivatives, but leading to significantly different catalytic performances [13–15]. For example, Cu^{II}/adeninato/carboxylato MOF (Cu^{II}/ade-MOF) nanosheets were converted to Cu nanoparticles, which obtained C_2H_4 with a maximum faradaic efficiency (FE) of 45% [16]. In another case, similar Cu nanoparticles were derived from semi-conductive MOF-$Cu_3(HITP)_2$, where a notable production C_2H_4 was observed attaining its maximum FE of 63% [17]. The phenomenon indicates that, before the C–C coupling process, there are other activation sites which critically influence catalytic efficiency.

Acutually, the structures of pristine MOF precursors still remain throughout the catalytic process, particularly in prolonged catalytic cases. In essence, pristine MOFs also harbor the capability to impact the CO_2RR process, even though they are commonly overlooked in discussions of the catalytic mechanism. We posit that the varied catalytic outcomes stemming from identical Cu-based derivatives are intricately linked to the presence of pristine MOFs. Unveiling the role of pristine MOFs can not only provide a new direction to design high-proformance MOF-based CO_2RR catalysts with minimize trial and error.

Constructing a rational catalytic system to explore the role of prinstine MOF precursors is still a significant challenge. On the one hand, to avoid variations in the C–C coupling efficiency in the second step, the derivatives produced by different Cu-based MOFs during the catalytic reaction should be completely identical [18,19]. On the other hand, to mitigate the influence of MOF's residual ligands, the prinstine MOFs chosen for comparsion should prossess the same chemical component but differet structures [20]. Last but not lesat, the MOFs catalysts should maintain the srtucture during the catalytic process, forming MOF-derivatives complexes rather than being entirely destroyed [21]. Therefore, to invesitigate a relationship between precursors and catalytic performance, it was es-

---

* Corresponding authors.
E-mail addresses: yafeili@njnu.edu.cn (Y. Li), guzhiyuan@njnu.edu.cn (Z.-Y. Gu).

[1] These authors contributed equally to this work.

https://doi.org/10.1016/j.cclet.2024.109937

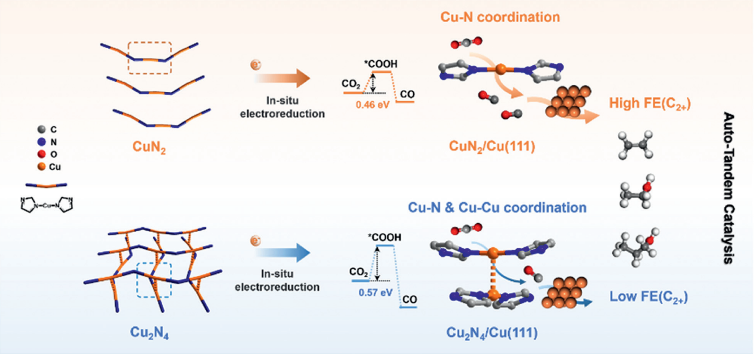

Scheme 1. The design of auto-tandem catalysts CuN_2/Cu(111) and Cu_2N_4/Cu(111) and the proposed CO_2RR catalytic mechanism.

sential to ensure structural similarity and stability as well as ligand consistency.

Here, two Cu(I) imidazole framework isomers with the identical formula $[Cu(imidazole)]_n$ were employed as the precursors, namely CuN_2 and Cu_2N_4 based on the coordination status. The only difference between the two precursors was the Cu coordination environments (Scheme 1). In the CuN_2 precursor, one Cu atom was linearly coordinated to N atoms of two imidazoles to form zig-zag one-dimensional chain. In the Cu_2N_4 precursor, two one-dimensional chains was perpendicularly stacked with a Cu-Cu bond formed bewteen the atoms of adjacent layers. The two Cu-based MOFs were both *in-situ* reconstructed to nanosized Cu(111) with a large number of MOFs retained under cathodic potential, named CuN_2/Cu(111) and Cu_2N_4/Cu(111), respectively. The CO_2RR performance of CuN_2, Cu_2N_4, CuN_2/Cu(111) and Cu_2N_4/Cu(111) was evaluated, respectively. The results showed that the both CuN_2 and Cu_2N_4 precursors produced CO while both CuN_2/Cu(111) and Cu_2N_4/Cu(111) produced C_{2+} products. The CuN_2 and Cu_2N_4 precursors showed a maximum FE_{CO} of 43.1% and FE_{CO} of 26.2% for the production of CO, respectively. Then, the CuN_2/Cu(111) and Cu_2N_4/Cu(111) exhibited a final $FE_{C_{2+}}$ of 64.8% and 43.9%, coorespondingly. The $FE_{C_{2+}}$ was closely related to the FE_{CO} of the pristine MOF precursors. We demonstrated a auto-tandem catalysis mechanism to reveal the performance of the Cu(imidazole) system. The pristine Cu(imidazole) played an activiation function to convert CO_2 into CO, and Cu(111) catalyzed CO to C_{2+} products. This auto-tandem catalysis mechanism was confirmed by TPD-CO, *in-situ* ATR-SEIRAS, and DFT computation. These results conclusively illustrated that pristine CuN_2 with more exposed Cu-N sites showed lower CO adsorption energy and generated higher CO substrate concentration, accelerating the formation of C_{2+} products. This rational mechanism provides a promising way and solution for the rational design of Cu-MOF catalysts.

The CuN_2 and Cu_2N_4 were prepared with the solvothermal method under different synthetic conditions according to the reported literature method [22,23]. The obtained yellowish and brownish powder was characterized with powder X-ray diffraction (PXRD), X-ray photoelectron spectroscopy (XPS), scanning electron microscopy (SEM), transmission electron microscopy (TEM), and high-resolution transmission electron microscopy (HRTEM). PXRD patterns showed that the synthetic materials were consistent with the simulated CuN_2 and Cu_2N_4, respectively. XPS results revealed that the oxidation state of CuN_2 was monovalent, and Cu_2N_4 exhibited primary monovalent and a little bit of bivalence due to additional Cu-Cu bonding (Fig. S1 in Supporting information). SEM images exhibited that both of them were block material piled up layer by layer, and the size reached the micrometer scale. The morphologies were also confirmed by HRTEM images. Besides, there had no crystal diffraction fringes from HRTEM images. The above characterizations revealed the pristine CuN_2 and Cu_2N_4 were successfully prepared and contained no Cu-based nanoparticles (Fig. S2 in Supporting information).

According to the previously reported method [24], under an electric field, the Cu-MOF underwent these processes of CO_2 adsorption, Cu reduction, Cu-N coordinated bond breaking, Cu atom restructuring, Cu nanoparticle growth, and nanoparticle aggregation. Therefore, we reconstructed CuN_2 and Cu_2N_4 by performing 1-h electrolysis from −0.78 V to −1.28 V *vs.* RHE. The reconstructed electrocatalysts were named as CuN_2/Cu(111) and Cu_2N_4/Cu(111), respectively. During the reconstruction process, we collected the electrochemical data and analyzed the products. Therein, gaseous products were quantified by an online gas chromatograph (GC), and liquid products were quantified by ^{1}H nuclear magnetic resonance spectroscopy (^{1}H NMR). Meanwhile, formate was detected with a high-performance liquid chromatograph (HPLC) (see details in Supporting information).

To evaluate the CO_2RR performance of CuN_2/Cu(111) and Cu_2N_4/Cu(111), we tested them in both H-cell and flow-cell. On the one hand, in H-cell, we measured linear sweep voltammetry (LSV) after 1-h electrolysis at −1.18 V *vs.* RHE in both CO_2 and N_2 saturated 0.1 mol/L KCl electrolyte (Fig. 1a). The CuN_2/Cu(111) exhibited lower onset potential and higher total current density (j_{total}) than Cu_2N_4/Cu(111) from −0.4 V to −1.2 V *vs.* RHE, illustrating better CO_2RR catalytic performance. Then, to choose applicable electrolyte, the two catalysts were tested in 0.1 mol/L $KHCO_3$, 0.5 mol/L $KHCO_3$ and 0.1 mol/L KCl electrolyte, respectively (Figs. S3 and S4 in Supporting information). The FE of various products for CuN_2/Cu(111) and Cu_2N_4/Cu(111) were calculated and compared. Obviously, the C_{2+} product selectivity in 0.1 mol/L KCl was far higher than 0.1 mol/L $KHCO_3$ and 0.5 mol/L $KHCO_{3.}$ Therefore, we chose 0.1 mol/L KCl electrolyte as the test condition in this work. For CuN_2/Cu(111), the C_{2+} products (C_2H_4, C_2H_5OH, and n-C_3H_7OH) were detected from −0.88 V *vs.* RHE (Figs. S5 and S6 in Supporting information). The maximum $FE_{C_{2+}}$ reached 64.8%, including $FE_{C_2H_4}$ of 41.5%, $FE_{C_2H_5OH}$ of 18.2%, and $FE_{n\text{-}C_3H_7OH}$ of 5.1% (Fig. 1b), which was middle level among reported Cu-based materials (Table S1 in Supporting information) [25-31]. For Cu_2N_4/Cu(111), the C_{2+} products were detected from −0.98 V *vs.* RHE. The maximum $FE_{C_{2+}}$ just reached 43.9%, including $FE_{C_2H_4}$ of 27.1%, $FE_{C_2H_5OH}$ of 12.6%, and $FE_{n\text{-}C_3H_7OH}$ of 3.4% (Fig. 1c). During the operated potential window from −0.98 V to −1.28 V *vs.* RHE, the FE_{C2+} of CuN_2/Cu(111) was higher than Cu_2N_4/Cu(111) (Fig. 1d). Besides, to evaluate the number of active sites of CuN_2/Cu(111) and Cu_2N_4/Cu(111), the electrical double-layer capacitor (C_{dl}) was measured in non-Faraday potential intervals with a different scan rate of cyclic voltammetry (CV) (Fig. S7 in Supporting information) [32-35]. The C_{dl} of CuN_2/Cu(111) was calculated as 1.02 mF/cm^2, higher than Cu_2N_4/Cu(111) of 0.32 mF/cm^2, indicating more ac-

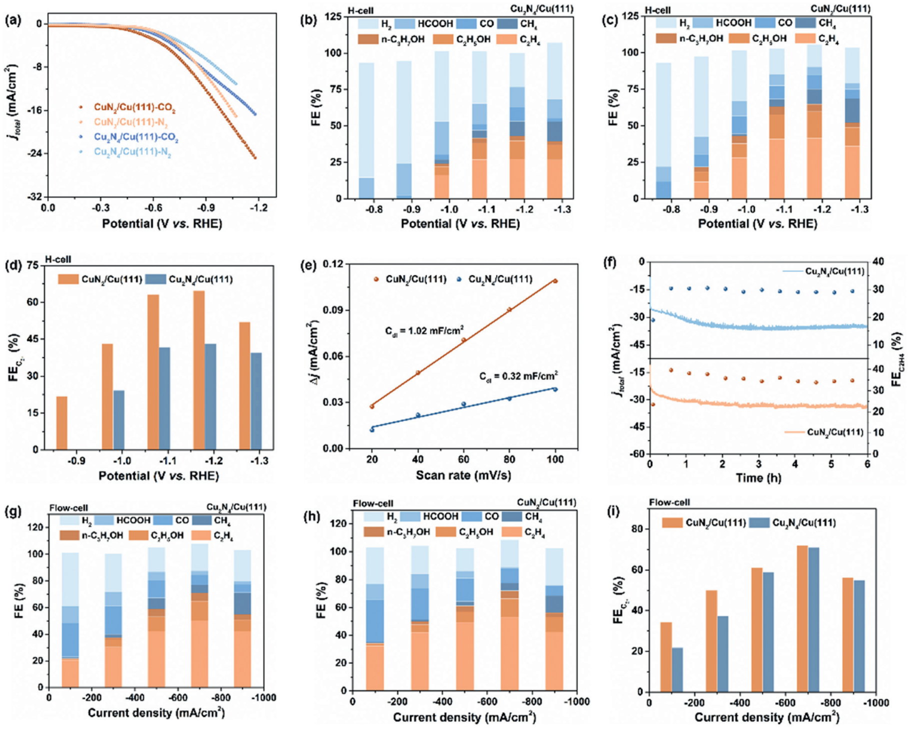

Fig. 1. (a) LSV curves of CuN_2/Cu(111) and Cu_2N_4/Cu(111) in both CO_2 and N_2 saturated 0.1 mol/L KCl electrolyte. FEs of various products at different operated potentialsl for (b) Cu_2N_4/Cu(111) and (c) CuN_2/Cu(111), respectively. (d) The comparison of $FE_{C_{2+}}$ for CuN_2/Cu(111) and Cu_2N_4/Cu(111) in H-cell. (e) C_{dl} measurements with CV method in non-Faraday potential interval under different scan rates. (f) Stability test at −1.18 V *vs.* RHE for 6-h electrolysis in H-cell. FEs of various products at different operated currents density in flow-cell for (g) Cu_2N_4/Cu(111), (h) CuN_2/Cu(111), respectively. (i) The comparison of $FE_{C_{2+}}$ for CuN_2/Cu(111) and Cu_2N_4/Cu(111) in flow-cell.

tive sites for CO_2RR (Fig. 1e). In addition, their stability was tested with online quantification of C_2H_4 (Fig. 1f). The $FE_{C_2H_4}$ and j_{total} were recorded during 6-h electrolysis. Both $FE_{C_2H_4}$ and j_{total} sharply increased from 5-min to 30-min electrolysis, illustrating the reconstruction of pristine CuN_2 and Cu_2N_4. Then, the FE_{C2H4} almost maintained, about 40% of CuN_2/Cu(111) and 30% of Cu_2N_4/Cu(111), showing good stability. Cu(imidazole) catalysts exhibit better stability than Cu-O based MOFs during CO_2RR process due to the more stable C–N coordination bond based on the hard and soft acid and base (HSAB) theory. According to the above results, it was obvious to conclude that the CO_2RR performance of CuN_2/Cu(111) was better than Cu_2N_4/Cu(111).

On the other hand, the CO_2RR performance of CuN_2/Cu(111) and Cu_2N_4/Cu(111) was also tested in flow-cell (Figs. 1g-i). The $FE_{C_{2+}}$ of CuN_2/Cu(111) and Cu_2N_4/Cu(111) were better than H-cell, where maximum was 72.1% and 71.0% at −700 mA/cm^2, respectively. Within the operated current range, the performance of CuN_2/Cu(111) was better than Cu_2N_4/Cu(111). The observed phenomenon from flow-cell was similar as in H-cell. Nevertheless, the difference in C_{2+} performance between the two catalysts less obvious than in H-cell, especially at high current density, this was owing to the destruction of pristine materials from the PXRD patterns (Fig. S12 in Supporting information). Therefore, we subsequently conducted material characterization and mechanism investigation under H-cell conditions with more stable three-phase reaction interface.

To reveal the actual catalytic sites during the above processes, the structure of CuN_2/Cu(111) and Cu_2N_4/Cu(111) was characterized by PXRD, XPS, Cu LMM Auger spectra, *in-situ* X-ray absorption near edge structure (XANES), *in-situ* X-ray emission spectroscopy (XES), HRTEM, and selected area electron diffraction (SAED), respectively (Fig. 2, Figs. S7, S8, S19 and S20 in Supporting information). PXRD patterns showed main diffraction peaks of pristine CuN_2 and Cu_2N_4 were retained (Fig. 2a), which was also observed from SEM images (Fig. S8). Meanwhile, the diffraction peaks of Cu(111) were detected at 43.2°. These results were further confirmed by HRTEM and SAED images (Figs. 2d and e). For CuN_2/Cu(111), HRTEM images showed the block of pristine CuN_2 piled up layer by layer, and some nanoparticles dispersed in it. The crystal spacing of these nanoparticles was measured as 0.209 nm of Cu(111). In addition, the bright diffraction spots of SAED images also confirmed that Cu(111) was a predominant crystal plane. The selective crystal plane derivatization may be attributed to the uniform Cu(I) distribution in the precursors. Furthermore, the Cu(111) plane was beneficial to promote the formation of C_{2+} products [36-38]. Similarly, the characterization and analysis for Cu_2N_4/Cu(111) were conducted (Fig. 2e). It showed pristine Cu_2N_4 was maintained with the formation of Cu(111) nanoparticles. It was worth noting that other very minor Cu species also existed in the two catalysts, such as 0.243 nm of Cu_2O(111). Therefore, the derivatives of CuN_2 and Cu_2N_4 were proved to be consistent, at the same time, the pristine materials were retained. Besides, the oxidation states of CuN_2/Cu(111) and Cu_2N_4/Cu(111) were investigated with Cu LMM, *in-situ* XANES and XES spectra. As shown in Fig. S9 (Supporting information), the main Cu LMM peak of both CuN_2/Cu(111) and Cu_2N_4/Cu(111) was recorded at the kinetic energy of 916.4 eV belonging to Cu(I), demonstrating the reservation of pristine CuN_2 and Cu_2N_4. Meanwhile, the Cu(0) peak with a kinetic energy of 918.8 eV was observed, indicating the reconstruction of Cu(imidazole). More convincingly, compared to pristine CuN_2 and Cu_2N_4, the *in-situ* XANES spectra of CuN_2/Cu(111) and Cu_2N_4/Cu(111) shifted to a low-energy region during the electrolysis, showing that the oxidation state of Cu(I) was reduced to Cu(0~I) (Fig. 2b). Besides, *in-situ* XES also exhibited the Cu oxidation state of pristine CuN_2 and Cu_2N_4 were reduced from OCP to −1.3 V *vs.* RHE (Fig. 2c). In especial, the reconstruction of CuN_2 was faster than Cu_2N_4, and the mixed Cu(0~I) was more than Cu_2N_4, these were what made the better catalytic performance of

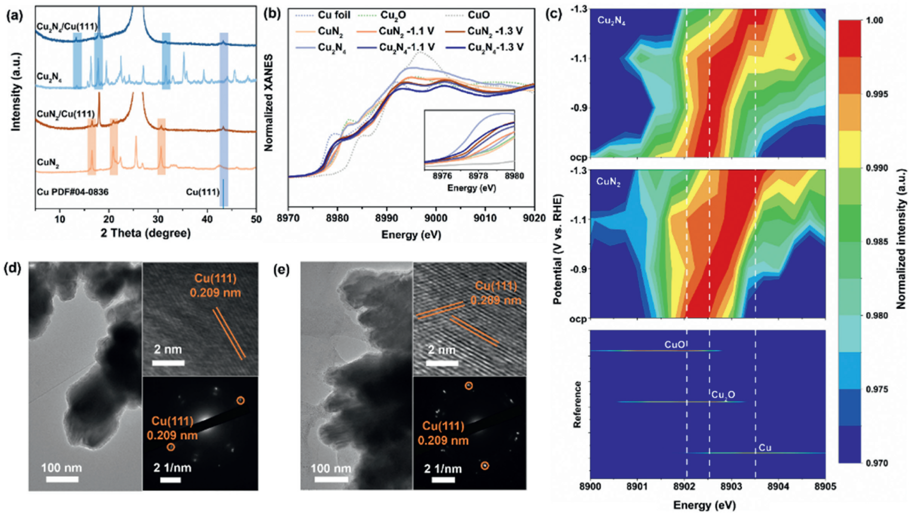

Fig. 2. The characterization of CuN_2/Cu(111) and Cu_2N_4/Cu(111) compared with pristine CuN_2 and Cu_2N_4. (a) PXRD patterns. (b) *In-situ* XANES spectra. The inset is enlarged part from 8975 eV to 8980 eV. (c) *In-situ* Cu K$\beta_{1,3}$ XES spectra from OCP to −1.3 V *vs.* RHE. OCP was open circuit potential. The microscopic analysis of (d) CuN_2/Cu(111) and (e) Cu_2N_4/Cu(111). The inset is HRTEM and SAED images.

derived CuN_2/Cu(111). Besides, both *in-situ* XANES and XES results demonstrated that pristine CuN_2 and Cu_2N_4 did not fully converted to metallic Cu. Therefore, the pristine materials played an important role in these auto-tandem catalysis. Furthermore, to demonstrate the stability of the catalysts, the structure of CuN_2/Cu(111) and Cu_2N_4/Cu(111) after the 6-h stability test was analyzed. PXRD patterns showed the main diffraction peaks of pristine CuN_2 and Cu_2N_4 were still retained (Fig. S10 in Supporting information). The diffraction peak of the Cu(111) derivative was observed, and the intensity was stronger than the materials after 1-h electrolysis, indicating a continuous reconstruction process during the stability test. The Cu(111) crystal plane was also identified from HRTEM and SAED images of CuN_2/Cu(111) and Cu_2N_4/Cu(111) (Fig. S11 in Supporting information).

According to the above structural characterizations, both the pristine Cu MOFs and the same derived Cu(111) existed during the catalytic process. Based on their different catalytic results, it was reasonable to speculate that both pristine Cu MOFs and derived Cu(111) acted as catalysts during the CO_2RR process. As Cu(111) usually reported for the C–C coupling to forming C_{2+} products, we supposed that the pristine Cu MOFs played an activation function to active CO_2, forming active substance for the next step of C–C coupling. This catalysis system with two steps was named as the auto-tandem catalysis system. The different catalytic performance of CuN_2/Cu(111) and Cu_2N_4/Cu(111) was possible came from the variation of coordination environment. Particularly, the Cu atom of pristine CuN_2 was just coordinated with two N atoms, while for Cu_2N_4, Cu was not only coordinated with two N atoms but also bonded with the other Cu atom of the adjacent layer. Therefore, we legitimately attributed the different catalytic performances to the different coordination environments of the pristine materials.

To reveal the role of coordination environment in MOF precursor, we first investigated the performance of sole CuN_2 and Cu_2N_4 by LSV and FE measurements, respectively. The LSV curve of pristine CuN_2 also showed lower onset potential and higher j_{total} than Cu_2N_4, indicating better catalytic performance (Fig. 3a). Then, to avoid catalyst reconstruction, short CO_2RR experiments with 50-s electrolysis were performed from −0.88 V to −1.18 V *vs.* RHE for CuN_2 and Cu_2N_4, and respective CO_2RR products were quantified. There were no C_{2+} products, and just CO and H_2 was detected for both CuN_2 and Cu_2N_4 (Fig. S13 in Supporting information). For pristine CuN_2, CO product was detected at −0.88 V *vs.* RHE, the FE_{CO} increased with potentials, and the maximum FE_{CO} reached up to 43.1% (Fig. 3b), which lies a medium level in the Cu-based materials with single metal site (Table S2 in Supporting information). Meanwhile, for pristine Cu_2N_4, the maximum FE_{CO} was only 24.4% (Fig. 3b). Obviously, the CO selectivity of pristine CuN_2 was much better than Cu_2N_4 during the whole operated potential window. These results illustrated the CO_2RR performance of pristine CuN_2, including onset potential and FE_{CO}, was better than Cu_2N_4.

To confirm the catalyst structure after 50-s electrolysis, the HRTEM, SEM, and PXRD characterizations were executed (Figs. S14-S16 in Supporting information). Both CuN_2 and Cu_2N_4 still exhibited pristine structures, and no Cu-based nanoparticles were observed. Therefore, the above catalytic performance factually reflected the ability of the pristine CuN_2 and Cu_2N_4 to convert CO_2. To establish a connection between MOF and Cu(111) in the auto-tandem catalysis system, we made comparison plots of FE_{CO} for the pristine materials and $FE_{C_{2+}}$ for the reconstructed materials at various potentials. As shown in Fig. 3c, both $FE_{C_{2+}}$ of CuN_2/Cu(111) and FE_{co} of CuN_2 were higher than Cu_2N_4/Cu(111) and Cu_2N_4, respectively. Therefore, the $FE_{C_{2+}}$ for reconstructed materials exhibited a positive correlation with FE_{CO} for the pristine materials.

According to some literatures, derived Cu metal was also known to convert CO_2 into C_{2+} products through CO as an intermediate. Therefore, in the auto-tandem catalysis system, it is very important to determine which of pristine MOF and the derived Cu(111) is the main active site for converting CO_2 to CO. On one hand, pristine CuN_2 and Cu_2N_4 were destructed under 8-h electrolysis tests at −1.18 V *vs.* RHE, which was fully reduced to Cu(111) from PXRD and SEM analysis (Fig. S17 in Supporting information). Subsequently, the derived Cu(111) was immediately tested to obtain FE_{CO} (Fig. 3d). After destruction, the derived Cu(111) exhibited lower FE_{CO} than pristine MOF from −0.98 V to −1.18 V *vs.* RHE. Especially at the potential of C_{2+} products, pristine CuN_2 and Cu_2N_4 played dominant active sites of converting CO_2 to CO. On the other hand, to explore the relationship between the two steps in the auto-tandem catalysis system, we compared the relative rates of CO_2 reduction to CO *vs.* CO reduction to C_{2+} products for the derived Cu(111) at −1.18 V *vs.* RHE. (Fig. 3e). All of the rates were around 2×10^{-7} mol min^{-1} cm^{-2}. The former is not much faster than the latter. Therefore, improving the rate of CO_2 reduc-

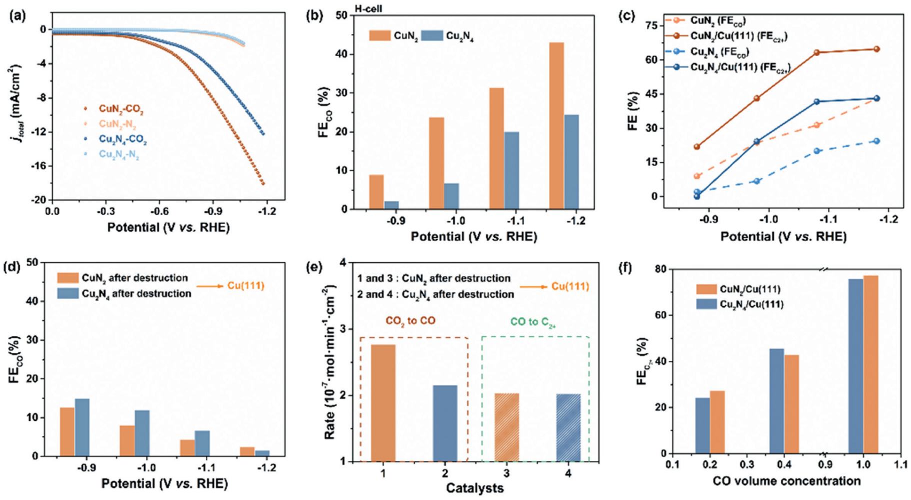

Fig. 3. (a) LSV curves of pristine CuN_2 and Cu_2N_4 in both CO_2- and N_2-saturated 0.1 mol/L KCl electrolyte. (b) FE_{CO} at different potentials with 50-s electrolysis for pristine CuN_2 and Cu_2N_4, respectively. (c) FEco for the pristine materials and $FE_{C_{2+}}$ for the reconstructed materials at various potentials. (d) After 8-h electrolysis tests for CuN_2 and Cu_2N_4 at −1.18 V *vs.* RHE, the pristine MOF was reduced to Cu(111), which was immediately tested to obtain FE_{CO}. (e) Relative rates of CO_2 reduction to CO *vs.* CO reduction to C_{2+} products for CuN_2 and Cu_2N_4 after 8-h electrolysis at −1.18 V *vs.* RHE. (f) CORR of CuN_2/Cu(111) and Cu_2N_4/Cu(111) at various CO volume concentrations with 1-h electrolysis under fixed −1.18 V *vs.* RHE.

tion to CO may promote C_{2+} products selectivity due to the rate-determining step of C–C coupling.

To further investigate the effect of the substrate CO on the C_{2+} product, control experiments of CO reduction reaction (CORR) with various CO volume concentrations were performed on CuN_2/Cu(111) and Cu_2N_4/Cu(111), respectively. The CO/N_2 mixture with CO volume concentrations of 0.2, 0.4, and 1 was employed instead of pure CO_2 for electrolysis. At these conditions, the CORR performance of CuN_2/Cu(111) and Cu_2N_4/Cu(111) was evaluated at a potential of −1.18 V *vs.* RHE. As shown in Fig. 3f, for the CO volume concentration of 0.2, 0.4, and 1, $FE_{C_{2+}}$ of CuN_2/Cu(111) was obtained as 27.3%, 42.9%, and 77.3%, respectively, while $FE_{C_{2+}}$ of Cu_2N_4/Cu(111) was 24.3%, 45.6%, and 75.9%, respectively. Therefore, the $FE_{C_{2+}}$ of CuN_2/Cu(111) and Cu_2N_4/Cu(111) significantly increased with CO volume concentration, illustrating that the CO concentration directly determines the C_{2+} product formation. Meanwhile, the obtained $FE_{C_{2+}}$ of CuN_2/Cu(111) and Cu_2N_4/Cu(111) was almost identical under the same CO volume concentration, revealing that CORR bypassed the first CO_2 activation step and only depended on the same active site, in this case, the Cu(111). Therefore, these results further demonstrated the rationality of the proposed auto-tandem catalysis mechanism.

To comprehensively reveal the role of pristine CuN_2 and Cu_2N_4 in the CO_2RR process, *in-situ* attenuated total reflection-surface enhanced infrared reflection absorption spectroscopy (*in-situ* ATR-SEIRAS) was conducted to monitor the intensity difference of *CO intermediate (Figs. 4a and b, Fig. S20) [39–44]. The IR spectrum was collected from open circuit potential (OCP) to −1.28 V *vs.* RHE. Notably, the *COOH intermediate was monitored at 1652 cm^{-1} and 1657 cm^{-1}, revealing the activation of CO_2. According to the literature [40,45], the band located in the region from 2000 cm^{-1} to 2100 cm^{-1} was attributed to the CO linear adsorption on the top sites of Cu surface (*CO), which was the key intermediate for subsequent C–C coupling step of C_{2+} products formation. On the one hand, for pristine CuN_2, the *CO intermediate with a wavenumber of 2057 cm^{-1} was observed at −0.68 V *vs.* RHE. Meanwhile, the intensity of *CO intermediate increased with the potentials, indicating faster conversion of CO_2 to *CO. The *CO stretching frequency shifted to a lower wavenumber as the potentials decreased from −0.68 V to −1.28 V *vs.* RHE owing to the Stark effect [45–47]. On the other hand, for pristine Cu_2N_4, the *CO intermediate was observed at a more negative potential of −0.98 V *vs.* RHE and a slightly lower wavenumber of 2037 cm^{-1} than CuN_2, indicating a higher energy barrier to obtain *CO intermediate. Meanwhile, to quantitatively compare the abilities of Cu sites in CuN_2 and Cu_2N_4 for the conversion of CO_2 into *CO, the *CO intermediate band intensities were plotted from −0.08 V to −1.28 V *vs.* RHE (Fig. 4c). Obviously, the *CO intermediate band intensity of CuN_2 was stronger than that of Cu_2N_4, and it significantly increased with an increase of potentials, which further supported that CuN_2 easily produced more *CO intermediates than Cu_2N_4.

Besides, the temperature-programmed desorption of CO (TPD-CO) technique was employed to investigate the chemisorption intensity of CO for pristine CuN_2 and Cu_2N_4 (Fig. 4d). Before testing TPD-CO, the thermogravimetric analysis (TGA) was conducted to determine the pyrolysis temperature of the catalysts (Fig. S21 in Supporting information). CuN_2 and Cu_2N_4 showed almost identical TGA curves, indicating that they were both thermally stable before about 250 °C. Therefore, we collected the TPD-CO data from 50 °C to 250 °C. According to the TPD-CO results, pristine CuN_2 exhibited a much lower CO desorption temperature of 148 °C than 207 °C of Cu_2N_4, indicating a lower desorption activation energy, which facilitated the *CO desorption and subsequent C–C coupling step on Cu(111) site.

Furthermore, to understand the different adsorption strength for intermediates during the CO_2RR process, we analyzed the density of state (DOS) for CuN_2 and Cu_2N_4. Especially, Cu 3d orbital partial density of state (PDOS) was conducted to calculate the d-band center which was regarded as the applicable descriptor to explain catalytic reactivity [48,49]. As shown in Fig. 4e, d-center value of CuN_2 and Cu_2N_4 were −1.4 eV and −2.9 eV, respectively. The position of d-band center for CuN_2 was closer to the Femi level (E_f) than Cu_2N_4, indicating stronger adsorption of intermediates [50]. Besides, the reaction pathway and energy barrier of *CO intermediate formation were explored with the DFT calculation [51–53]. The Cu sites of pristine CuN_2 and Cu_2N_4 were modeled as the active sites for CO production. The whole reaction pathway from CO_2 to CO was proposed as follows (Fig. 4f) [44]: $CO_2 \rightarrow {}^*COOH \rightarrow {}^*CO \rightarrow CO$, where the first step $CO_2 \rightarrow {}^*COOH$ was the rate-determining step (RDS). Meanwhile, the intermediates such as *COOH and *CO were also detected with *in-situ* ATR-SEIRAS spectroscopy. The RDS reaction energy of pristine CuN_2 was calcu-

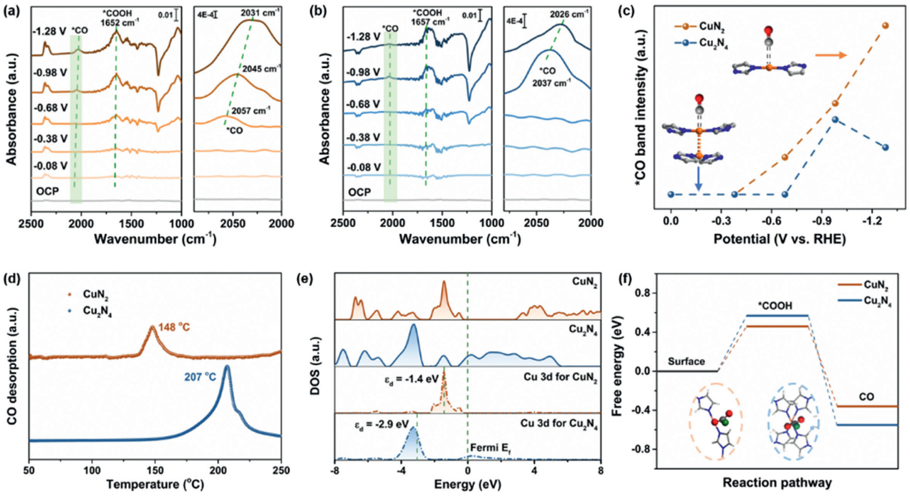

Fig. 4. *In-situ* ATR-SEIRAS results of (a) CuN_2 and (b) Cu_2N_4. On the right were the enlarged spectra from 2090 cm^{-1} to 2000 cm^{-1}. OCP was open circuit potential. (c) *CO band intensity of CuN_2 and Cu_2N_4 from (a) and (b) at different potentials. (d) TPD-CO curve for CuN_2 and Cu_2N_4. (e) DOS calculations of CuN_2 and Cu_2N_4. (f) Gibbs free energy profiles for CO production on CuN_2 and Cu_2N_4. The inset images were the DFT calculation structure model of *COOH adsorbed on Cu site for CuN_2 and Cu_2N_4.

lated as 0.46 eV, which was lower than pristine Cu_2N_4 with 0.57 eV. These results further demonstrated that the pristine coordination environment of Cu(imidazole) catalysts played a decisive role in CO generation, thus affecting further C_{2+} production.

In summary, we uncovered that the pristine Cu(imidazole) played an critical activation function to convert CO_2 into CO, and subsequent the *in-situ* derived Cu(111) acted as the active sites for C–C coupling. This auto-tandem catalysis activity was closely related to the coordination environment of the pristine MOFs. CuN_2 with more exposed Cu-N sites showed higher ability to form CO, thus the CuN_2/Cu(111) exhibited higher C_{2+} selectivity. The catalytic active sites were explored with HRTEM, SAED, XPS, and XANES techniques. This mechanism was demonstrated with CORR control experiment, TPD-CO, *in-situ* ATR-SEIRAS, and DFT calculation. We anticipate that the auto-tandem catalysis mechanism will be utilized in the design and development of Cu-based MOF precursors for promoting the C_{2+} products selectivity of reconstructed catalysts. The key of applying the auto-tandem catalytic mechanism is to improve the intrinsic catalytic active and stability of pristine MOF.

CRediT authorship contribution statement

Xiang-Da Zhang: Conceptualization, Data curation, Formal analysis, Writing – original draft. **Jian-Mei Huang:** Data curation. **Xiaorong Zhu:** Software. **Chang Liu:** Investigation. **Yue Yin:** Investigation. **Jia-Yi Huang:** Investigation. **Yafei Li:** Supervision, Validation. **Zhi-Yuan Gu:** Funding acquisition, Supervision, Visualization, Writing – review & editing.

Acknowledgments

This work is supported by the National Natural Science Foundation of China (Nos. 22174067 and 22204078), the Natural Science Foundation of Jiangsu Province of China (No. BK20220370), Jiangsu Provincial Department of Education (No. 22KJB150009), State Key Laboratory of Analytical Chemistry for Life Science (No. SKLACLS2218), and the Priority Academic Program Development of Jiangsu Higher Education Institutions. The authors would like to thank BL11B, BL14W1, and BL17B in Shanghai Synchrotron Radiation Facility (SSRF) and BL01B in National Synchrotron Radiation Laboratory (NSRL).

Supplementary materials

Supplementary material associated with this article can be found, in the online version, at doi:10.1016/j.cclet.2024.109937.

References

[1] J. Liu, D. Yang, Y. Zhou, et al., Angew. Chem. Int. Ed. 60 (2021) 14473–14479.
[2] D.H. Nam, O. Shekhah, G. Lee, et al., J. Am. Chem. Soc. 142 (2020) 21513–21521.
[3] X.F. Qiu, H.L. Zhu, J.R. Huang, et al., J. Am. Chem. Soc. 143 (2021) 7242–7246.
[4] J.X. Wu, S.Z. Hou, X.D. Zhang, et al., Chem. Sci. 10 (2019) 2199–2205.
[5] A.M. Appel, J.E. Bercaw, A.B. Bocarsly, et al., Chem. Rev. 113 (2013) 6621–6658.
[6] S. Nitopi, E. Bertheussen, S.B. Scott, et al., Chem. Rev. 119 (2019) 7610–7672.
[7] L. Majidi, A. Ahmadiparidari, N. Shan, et al., Adv. Mater. 33 (2021) 2004393.
[8] T. Ahmad, S. Liu, M. Sajid, et al., Nano Res. Energy 1 (2022) e9120021.
[9] X. Han, Z. Liu, M. Cao, et al., Chem. Mater. 34 (2022) 6713–6722.
[10] C. Kong, G. Jiang, Y. Sheng, et al., Chem. Eng. J. 460 (2023) 141803.
[11] J. Wang, Y. Zhang, Y. Ma, et al., ACS Mater. Lett. 4 (2022) 2058–2079.
[12] X. Tan, C. Yu, C. Zhao, et al., ACS Appl. Mater. Interfaces 11 (2019) 9904–9910.
[13] M.K. Kim, H.J. Kim, H. Lim, et al., Electrochim. Acta 306 (2019) 28–34.
[14] M.R. Smith, A. Gilman, C.W. Hullfish, et al., J. Phys. Chem. C 126 (2022) 13649–13659.
[15] Z. Weng, Y. Wu, M. Wang, et al., Nat. Commun. 9 (2018) 415.
[16] F. Yang, A. Chen, P.L. Deng, et al., Chem. Sci. 10 (2019) 7975–7981.
[17] H. Sun, L. Chen, L. Xiong, et al., Nat. Commun. 12 (2021) 6823.
[18] Y. Zhao, L. Zheng, D. Jiang, et al., Small 17 (2021) 2006590.
[19] Q. Zhu, D. Yang, H. Liu, et al., Angew. Chem. Int. Ed. 59 (2020) 8896–8901.
[20] N. Li, P. Yan, Y. Tang, et al., Appl. Catal. B 297 (2021) 120481.
[21] D. Yao, T. Cheng, A. Vasileff, et al., Angew. Chem. Int. Ed. 60 (2021) 18178–18184.
[22] Y.Q. Tian, H.J. Xu, L.H. Weng, et al., Eur. J. Inorg. Chem. 2004 (2004) 1813–1816.
[23] X.C. Huang, J.P. Zhang, Y.Y. Lin, et al., Chem. Commun. (2004) 1100–1101.
[24] T. Bao, W. Zhai, C. Yu, et al., Small Struct. 5 (2024) 2300293.
[25] Y. Li, Z. Pei, D. Luan, et al., Angew. Chem. Int. Ed. 62 (2023) e202302128.
[26] Y. Baek, H. Song, D. Hong, et al., J. Mater. Chem. A 10 (2022) 9393–9401.
[27] Z. Li, Y. Fang, J. Zhang, et al., J. Mater. Chem. A 9 (2021) 19932–19939.
[28] L. Fan, C. Xia, F. Yang, et al., Sci. Adv. 6 (2020) eaay3111.
[29] A. Handoko, C. Ong, Y. Huang, et al., J. Phys. Chem. C 120 (2016) 20058–20067.
[30] A. Loiudice, P. Lobaccaro, E.A. Kamali, et al., Angew. Chem. Int. Ed. 55 (2016) 5789–5792.
[31] D. Kim, C.S. Kley, Y. Li, et al., Proc. Natl. Acad. Sci. U. S. A. 114 (2017) 10560–10565.
[32] Y. Sha, J. Zhang, X. Cheng, et al., Angew. Chem. Int. Ed. 61 (2022) e202200039.
[33] J. Yuan, S. Chen, Y. Zhang, et al., Adv. Mater. 34 (2022) 2203139.
[34] Y. Li, S.L. Zhang, W. Cheng, et al., Adv. Mater. 34 (2022) 2105204.
[35] Y. Zou, C. Liu, C. Zhang, et al., Nat. Commun. 14 (2023) 5780.
[36] T. Yan, P. Wang, W.Y. Sun, Small 19 (2023) 2206070.
[37] H. Xiao, T. Cheng, W.A. Goddard III, J. Am. Chem. Soc. 139 (2017) 130–136.
[38] Z.-H. Zhao, K. Zheng, N.-Y. Huang, et al., Chem. Commun. 57 (2021) 12764–12767.
[39] B.r. Ratschmeier, B.r. Braunschweig, J. Phys. Chem. C 125 (2021) 16498–16507.
[40] J. Heyes, M. Dunwell, B. Xu, J. Phys. Chem. C 120 (2016) 17334–17341.
[41] H. Wang, Y.W. Zhou, W.B. Cai, Curr. Opin. Electrochem. 1 (2017) 73–79.
[42] H. Guo, D.H. Si, H.J. Zhu, et al., Angew. Chem. Int. Ed. 63 (2024) e202319472.
[43] Q.J. Wu, D.H. Si, Q. Wu, et al., Angew. Chem. Int. Ed. 62 (2023) e202215687.

[44] H.J. Zhu, D.H. Si, H. Guo, et al., Nat. Commun. 15 (2024) 1479.
[45] H. Miyake, M. Osawa, Chem. Lett. 33 (2004) 278–279.
[46] D.K. Lambert, Electrochim. Acta 41 (1996) 623–630.
[47] A. Wuttig, C. Liu, Q. Peng, et al., ACS Central. Sci. 2 (2016) 522–528.
[48] S. Jiao, X. Fu, H. Huang, Adv. Funct. Mater. 32 (2022) 2107651.
[49] E. Santos, W. Schmickler, ChemPhysChem 7 (2006) 2282–2285.
[50] Q. Zhang, L. Guo, J. Clust. Sci. 29 (2018) 867–877.
[51] G. Kresse, J. Hafner, Phys. Rev. B 47 (1993) 558–561.
[52] K. Kim, P. Wagner, K. Wagner, et al., Energy Fuel 36 (2022) 4653–4676.
[53] J. Wang, L. Gan, Q. Zhang, et al., Adv. Energy Mater. 9 (2019) 1803151.